



Influence of TiO₂ on Intragranular Acicular Ferrite Nucleation in Low-Carbon Steel

Weiying Huang¹ · Qiuping Li² · Aojia Li³

Received: 28 September 2023 / Accepted: 4 January 2024 / Published online: 14 February 2024
© The Indian Institute of Metals - IIM 2024

Abstract Oxide metallurgy technology uses inclusion to induce intragranular acicular ferrite (IAF). The purpose is to refine the steel's organization and improve its strength. However, the mechanism that inclusion induces IAF nucleation is still unclear. To solve this problem, we added TiO₂ into the low-carbon steel to investigate the ferrite nucleation mechanism induced by Ti inclusions by SEM, TEM, and EPMA. The results show that TiO₂ was added to the molten steel to form composite inclusions TiN–MnS–3MnO·Al₂O₃·3SiO₂–Ti₃O₅ by temperature control. These inclusions are effective in inducing IAF nucleation. It is consistent with the depletion zone mechanism and low mismatch degree mechanism. It is attributed to MnS inclusions in the composite inclusions and Mn elements in the solute poverty zone. The mismatch strain between TiN–MnS–3MnO·Al₂O₃·3SiO₂–Ti₃O₅ and IAF is less than 6%. The in-depth study of the mechanism of induced IAF nucleation by containing Ti inclusions is conducive to promoting the progress of oxide metallurgy technology.

Keywords Oxide metallurgy technology · Intragranular acicular ferrite · TiO₂ · Low lattice matching · Inclusions

1 Introduction

Oxide metallurgy technology [1–4] uses fine dispersed inclusions to induce intragranular acicular ferrite (hereafter IAF) nucleation. The aim is to refine the structure and improve the performance of low-carbon steel. Ferrite microstructure, the product of intragranular nucleation on inclusions, has been reported to improve resistance to cracking and be beneficial for achieving high toughness by forming an interlocking structure that reduces effective grain size [5]. Thus, the development of minuteness ferrite is recognized as a key technology to enhance the toughness of low-carbon steel. Hitherto, there are three generations of oxidation metallurgy: Firstly, using the dispersed TiN particles pins austenite to refine the welding of heat-affected zone structure; furthermore, TiO_x inclusions facilitate IAF nucleation to refine the structure of the steel; at present, the third generation mainly uses composite inclusions such as magnesium, calcium sulfide, and oxide to promote IAF formation. Titanium compounds were used in the first and second generations of oxide metallurgy, and many titanium compounds were included in the study of the third generation of composite inclusions.

At present, composite inclusions containing Ti have been studied more for inducing IAF nucleation. However, there is still unity on the mechanism of IAF nucleation induced by containing Ti inclusions. It is one of the reasons that hinder the progress of oxide metallurgy technology. Three nucleation mechanisms for inclusions inducing IAF nucleation are as follows [6–9]:

- (1) Mn-depleted zone.
- (2) The stress–strain energy.
- (3) Low lattice matching.

✉ Qiuping Li
20220901067@stu.cqu.edu.cn

¹ Department of Material Engineering, Hebei Vocational University of Industry and Technology, Shijiazhuang 050091, Hebei, People's Republic of China

² College of Materials Science and Engineering, Chongqing University, Chongqing 400044, People's Republic of China

³ Bozhou University College of Traditional Chinese Medicine, Bozhou 236000, Anhui, People's Republic of China

These three factors depend on the composition and structure of the inclusion. Accordingly, in the present study, each of these three factors responsible for the inclusion potency for IAF nucleation was evaluated simultaneously, and the contribution of each factor was considered. Table 1 shows the recent research on titanium inclusions inducing IAF. According to Table 1, there are few studies on the nucleation mechanism of IAF induced by the Ti composite inclusions. And the mechanism of containing Ti inclusions inducing IAF nucleation is not uniform.

In this work, TiO_2 was added to low-carbon steel, and IAF was induced by controlling the cooling temperatures. The mechanism of induced IAF nucleation was systematically investigated by scanning electron microscope (SEM), transmission electron microscopy (TEM), and electron probe micro-analyzer (EPMA) analysis. Three current mechanisms (Mn-depleted zone, stress-strain energy, and low lattice matching between ferrite and inclusions) were discussed. That provides a theoretical basis for refining the grain structure to advance oxide metallurgy.

2 Preparation of Materials

2.1 Materials Synthesis

Low-carbon steel was studied as the base material. The samples were heated up to 1538 °C, held for 20 min, and mixed with known properties TiO_2 . Figure 1 shows the experimental temperatures. Stirring with a corundum bar had a significant promoting effect of mechanical force on molten steel and TiO_2 . This operation could ensure that TiO_2 particles were added in the heat preservation process. Then, the samples were cooled to ambient temperature. The heating and

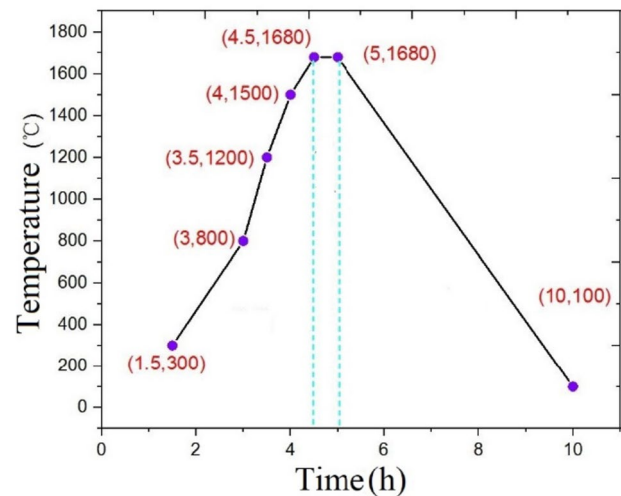


Fig. 1 Experimental temperatures

cooling process was conducted in an infrared furnace under ultra-high-purity argon (> 99.0%). The chemical compositions of sample 2 with TiO_2 additions are listed in Table 2.

2.2 Materials Characterization

An automatic metallurgical microscope (DMI-5000M, Leica) was used to observe the structure of the sample and then, a field emission scanning electron microscope (FE-SEM; S-4800, JEOL) for microstructure observation and inclusion component detection. Line scans of typical inclusion compositions were detected by SEM-EDS. The limit of SEM-EDS detection is 0.1%, and the resolution ratio is 1–3 nm. As we all know, EMPA-EDS detection reaches 0.01%, though its resolution ratio is only 5 nm. In order to

Table 1 References of titanium inclusion inducing IAF

Inclusion types	Nucleation mechanism	Refs.
Ti_2O_3	–	[7–11]
TiO	Low lattice misfit	[12–14]
TiN	–	[12, 15–17]
TiO, TiO_2 , Ti_3O_5	Mn-depleted zone	[7]
Ti_3O_5 -MnS	Mn-depleted zone	[18, 19]
TiN-MnS	Mn-depleted zone	[20–22]
Ti_2O_3 -TiN	Low lattice misfit	[22, 23]
Ti_xO -MnS	–	[24, 25]
Ti_2O_3 - Al_2O_3 -TiN	–	[26]
Al-Ti-Mn-Cu-S-O	–	[27]
MgO- Al_2O_3 - Ti_2O_3 -MnS	–	[28–30]
MgO- Al_2O_3 -TiO _x -SiO ₂ -MnS	Mn-depleted zone	[31]
MnO- Al_2O_3 -SiO ₂ -TiO _x -MnO	Mn-depleted zone	[32]
Ti-Zr-Mn-O-S-TiN	Low lattice misfit	[33]
MgO- Ti_2O_3 -MnO- Al_2O_3 -MnS-CaS-TiN	–	[34]

Table 2 Chemical compositions of samples (wt%)

No	Element	C	Mn	S	P	Si	Als	Ti
Sample 1	Contents	0.072	1.250	0.085	0.016	0.339	0.0697	0.017
Sample 2	Contents	0.070	1.220	0.080	0.015	0.320	0.066	0.030

confirm the truth of the solute poverty zone, we used the mapping of EMPA–EDS to test the typical inclusion. It is more accurate using both integrated analyses. To investigate the nucleation mechanism between the typical inclusions and IAF, TEM (JEM-2800F, JEOL) sample preparation using a dual-beam focused ion beam system (DB-FIB; JEM-2800F, FEI) was used. The Ga ion beam was used for cutting at 30 kV accelerating voltage, and the cut sample was put into copper mesh and coated with Pt film of about 1 μm thickness. TEM analysis was conducted, and selected area electron diffraction (SAED) patterns acquired from high-resolution electron microscopy (HREM) images were also analyzed.

2.3 Materials Properties

There are three kinds of TiO_2 crystal structures: anatase, rutile, and brookite. When the temperature exceeds 800 $^\circ\text{C}$, anatase and brookite transform into rutile. Therefore, TiO_2 inclusions can be directly considered as rutile for research in the steel smelting process. The melting point of rutile TiO_2 is 1850 $^\circ\text{C}$, which is higher than the melting point of molten steel. The Ti–O bond is short and unstable, which is easy to reunite when the temperature rises. Thus, it can reduce the specific surface area and increase the adsorption. It is easy to combine with TiO_2 in adsorption for molten steel at 1600 $^\circ\text{C}$. Nano-scale TiO_2 has a small particle size and high surface energy. It is easy to agglomerate to form secondary particles while adding molten steel. The early study [35] showed that when the content of TiO_2 was less than 1%, the phenomenon of agglomeration was unlikely to occur. To eliminate the influence of other forces and factors, TiO_2 was fully added to the molten steel, the content was selected as 1%, and the size was 10 μm .

3 Results and Discussion

3.1 Characteristics of Microstructure Morphology and Inclusions

Figure 2 shows the results of morphology, size, and the number of inclusions in samples 1 and 2. It can be seen that the addition of TiO_2 significantly increases the size of inclusions in steel in the range of 1–3 μm . Inclusions are predominantly spherical. And the number of spherical inclusions increases. It is initially hypothesized that there is a

polymerization growth of inclusions after the addition of TiO_2 . The microstructure morphology of samples 1 and 2 with TiO_2 is shown in Fig. 3. It can be seen that sample 1 is mainly composed of intragranular polygonal ferrite (IPF) containing fine inclusions and some pearlite. The grain size of IPF is about 100 μm . There are two types of IGF: IAF and IPF in sample 2. Most of IAF are nucleated and precipitated by inclusions. A noticeable phenomenon shows that new secondary nucleating ferrites are nucleated by primary ferrites. Secondary ferrite-related studies have been published in the literature [36]. IAF grows freely in large-angle and multi-dimensional competition to form an interwoven or cross-hatched structure. The experimental results infer that the whole microstructure consists of secondary nucleating ferrite and inclusions inducing IAF to refine grains.

The inclusion of the nuclei of IPF in sample 1 is displayed in Fig. 4. It can be observed from the microscopic morphology that the inclusion has a gap with ferrite. In Sample 2 (Fig. 5), the morphology of inclusion, regular circle, as IAF nucleation core differs from sample 1. The center is off-white, and the outer is covered with black materials. The connection between it and IAF is relatively close. Judging from the EDS results, it is evident that two kinds of inclusion are composed of the same elements: O, Mn, Si, S, Al, and Ti. Compared with them, the proportions of other elements are similar, except that Ti elements in sample 2 significantly increase from 1.38% to 10.32%. TiO_2 was successfully added to molten steel. They react with the original inclusions and then aggregate into the secondary particles to induce IAF.

3.2 Mn-depleted Zone

In low-carbon steel, it has been generally agreed that an increase in the chemical driving force due to the local depletion of some elements near an inclusion promotes the development of acicular ferrites, such as Mn, C, and Al. We investigated the solute deficiency to understand how the compound inclusions with TiO_2 induce IAF.

The linear scanning function in SEM–EDS detected the relationship between inclusion distance and density (one data every 0.1 μm and the scanning time was more than 60 s). This method considers the influence of electron beam size and counting rate. It qualitatively reacts to the composition changes of inclusion. Figure 6 is a lining image for inclusion inducing IAF made up of O–Mn–Si–S–Al–Ti. It can be seen that Mn contents near 1.25 μm to 6.26 μm increase sharply, reaching the range of 20% and 24%. It is

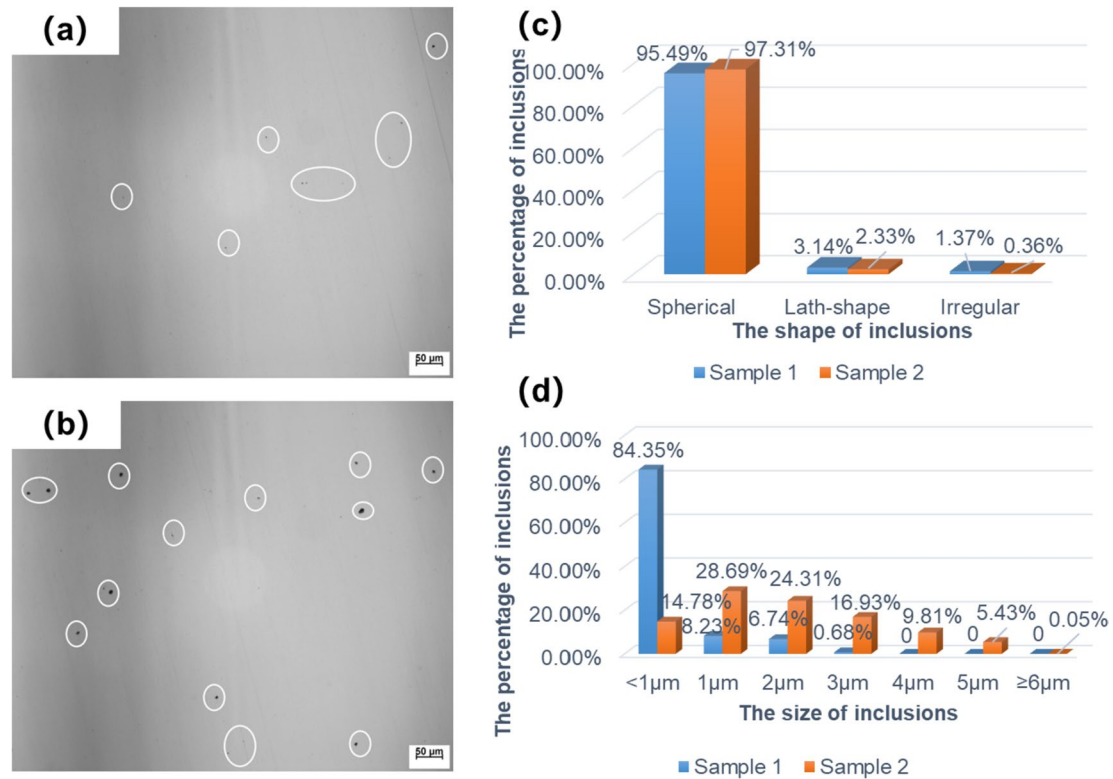


Fig. 2 Results of morphology, size, and the number of inclusions in samples 1 and 2: **a** the morphology of sample 1; **b** the morphology of sample 2; **c** the shape of inclusions; **d** the size of inclusions

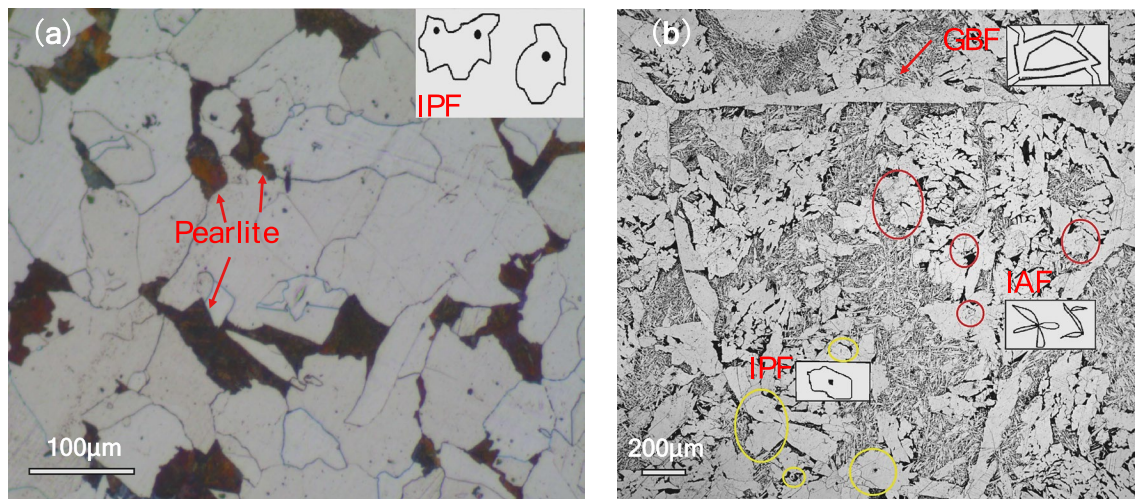


Fig. 3 Microstructure morphology of steel: **a** sample 1. **b** sample 2 with TiO_2

worth noticing sharp changes up and down in the distance of 1.25 μm and 2.8 μm . Therefore, such inclusions exist in the solute poverty zone, which can be judged to be caused by Mn elements. Besides, the same elements can appear in multiple positions in one inclusion.

In order to confirm the truth of the solute poverty zone, we used the mapping of EMPA-EDS to test the typical inclusion. It is more accurate using both integrated analyses. The inclusion was analyzed as large as 6 μm in EMPA (Fig. 7). The composition diagram of inclusions is Fig. 7i. The central element is a combination of Al–Si–Mn–O, which could

Fig. 4 SEM analysis results for sample 1

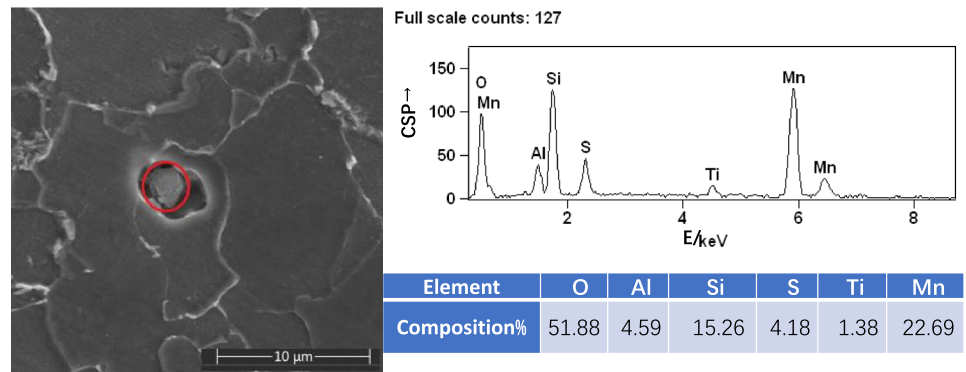


Fig. 5 SEM analysis results for sample 2

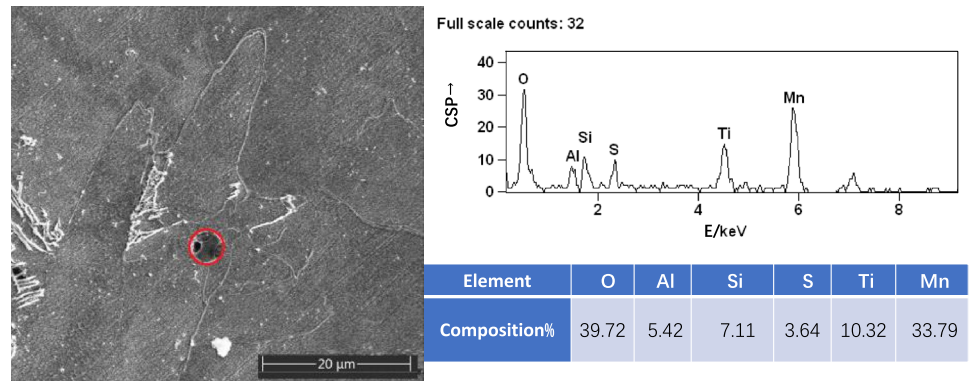
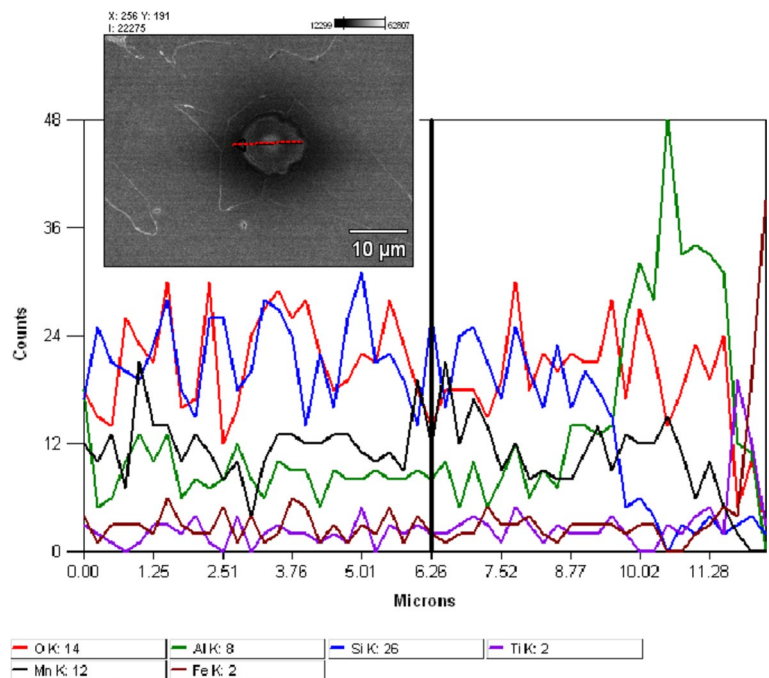


Fig. 6 SEM–EDS elemental lining image for inclusion inducing IAF



be judged as a typical Al_2O_3 – MnO – SiO_2 composite inclusion surrounded by MnS , TiN , and minute quantity titanium oxide. Si elements in the core location can be up to 80%. Al elements have a partial concentration of element solute

in the whole inclusion edge, even though some areas are as high as 68%. Mn contents are full of the entire inclusion, and the region with the highest inclusion, up to 50%, is the MnS inclusion wrapped in the periphery. Comparatively,

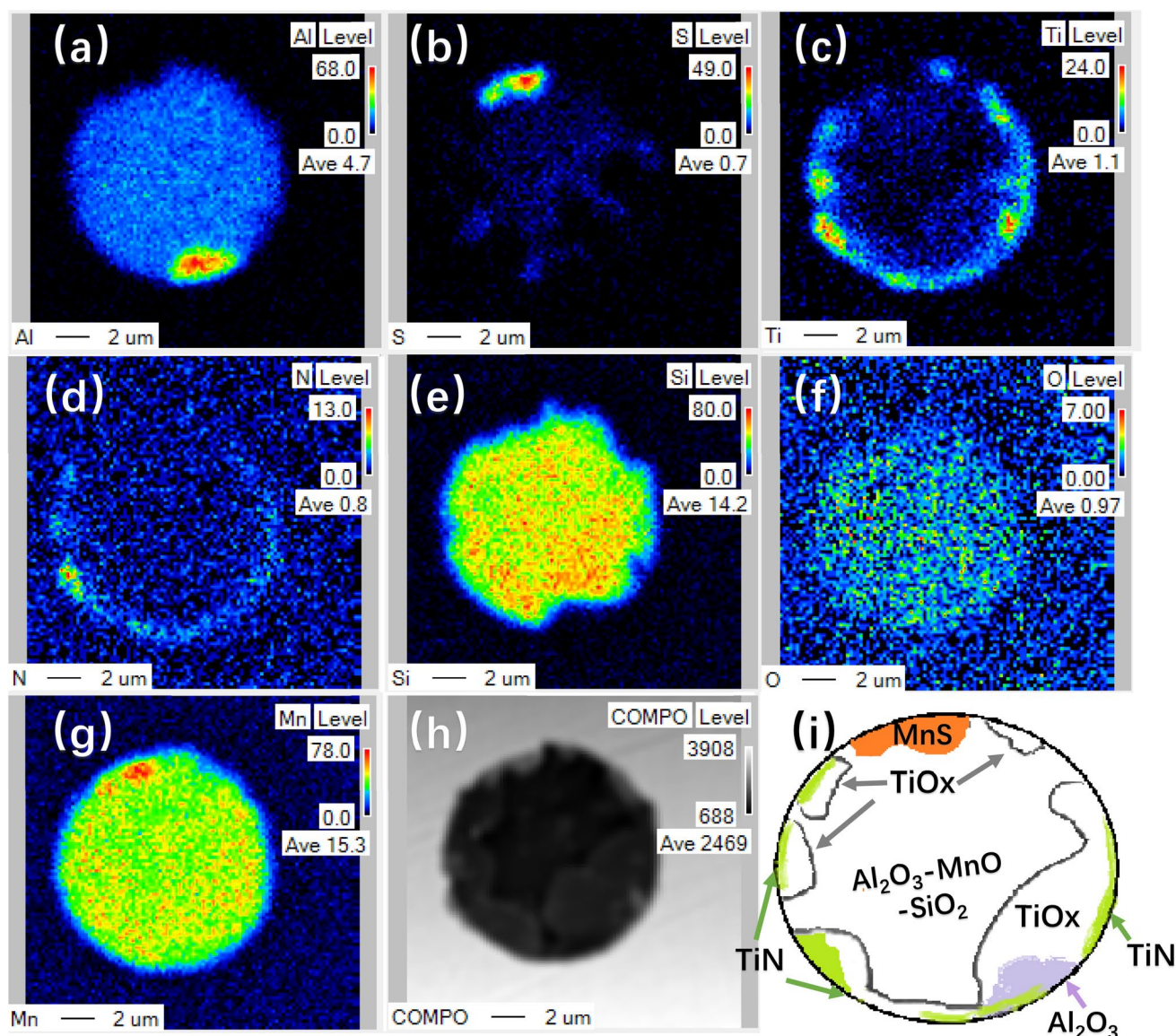


Fig. 7 EPMA analysis of one typical inclusion effective for IAF nucleation. **a–g** chemical maps of different elements. **h** morphology of Inclusion. **i** schematic diagram of inclusion composition

Mn elements are less in steel than inclusions. Furthermore, it can be seen that the contents of Ti in this large-size inclusion are significantly increased, up to 24% at the highest, mainly composed of TiN and titanium oxides. That means TiN and titanium oxides wrap in the outermost layer of the entire inclusion. IAF was found to nucleate on MnS + TiN inclusions, as previously reported by Hou et al. [23].

SEM-EDS lining and EPMA-EDS mapping analysis display Mn segregation to conform to the solute depletion mechanism. The process of non-metallic inclusions and new phase formation during the solidification of molten steel is realized by relative movement between atoms. They need to rely on energy fluctuation to overcome the activation energy to produce relative movement between atoms. This process

is also called diffusion. The smaller the activation energy of atoms reaching a new position, the more they can diffuse. From Figs. 6 and 7, it can be concluded that Mn solute-poor zone joint compound inclusions and IAF. Equation (1) [37] can be used to analyze the process of IAF formation induced by the Mn solute poverty zone:

$$D_A^{gb} = D_A^0 \exp\left(-\frac{Q_A^{gb}}{RT}\right) \quad (1)$$

D_A^{gb} : interfacial diffusion coefficient of matter (cm^2/s); D_A^0 : aggregate diffusion coefficient of A substances (cm^2/s); Q_A^{gb} : A interfacial diffusion activation energy (KJ/mol); R: the gas constant is $8.314 \times 10^{-3} \text{kJ mol}^{-1} \text{K}^{-1}$; T: temperature (K).

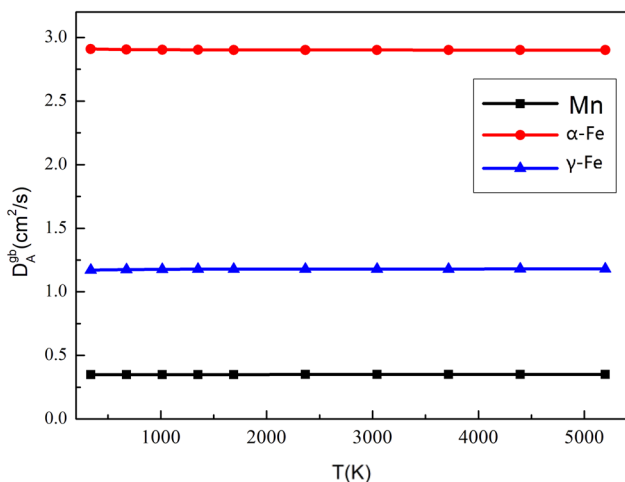


Fig. 8 D_A^{gb} of Mn, Al, α -Fe, γ -Fe

Table 3 Value of Mn, α -Fe, γ -Fe [38, 39]

Material	Mn	α -Fe	γ -Fe
D_A^0 (cm ² /s)	0.35	1.9	0.18
Q_A^{gb} (KJ/mol)	174	239	270

Fig. 9 Formation process of Mn-depleted zone

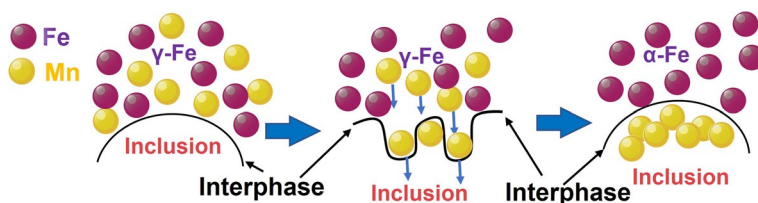


Figure 8 is obtained by calculating the data in Table 3 and Eq. (1). It can be concluded that the diffusion activation energy of Mn atoms is less than that of Fe. The diffusion coefficient is small, so the diffusion rate is large. Figure 9 is a schematic diagram of Mn elements solute depletion in the formation process. On the grain boundary Fe matrix and inclusion, the Mn elements in the γ -Fe matrix are more likely to diffuse and aggregate to the inclusions, resulting in interfacial migration. As the diffusion of Mn atoms proceeds, γ -Fe transforms into α -Fe. The inclusion and the steel interface intersection are placed to form the Mn-depleted zone, and the inclusion is MnS. Meanwhile, the IAF forms.

3.3 Low Lattice Misfit

Figure 10 shows the TEM detection results of IAF induced by Ti inclusions contained. The main elements are O, Al, Si, S, Ti, Mn, and C in the sample 2. The inclusion compositions are 3MnO Al₂O₃ SiO₂, MnS, TiN, and Ti₃O₅ from the following analyses Figs. 11, 12, and 13. In order to make clear the relationship between the composition and microstructure of the inclusion, we enlarged the sample to explore it in depth.

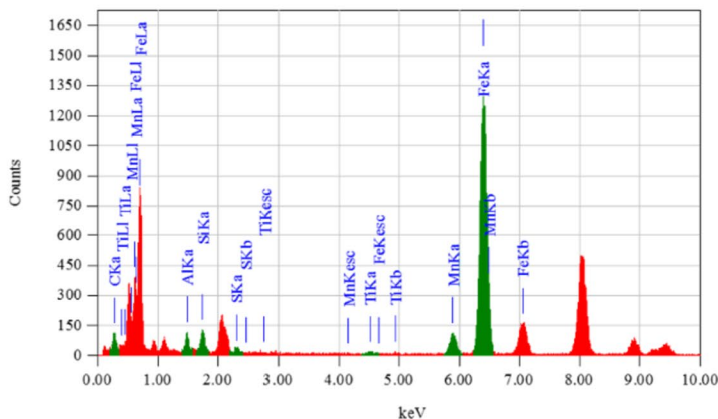
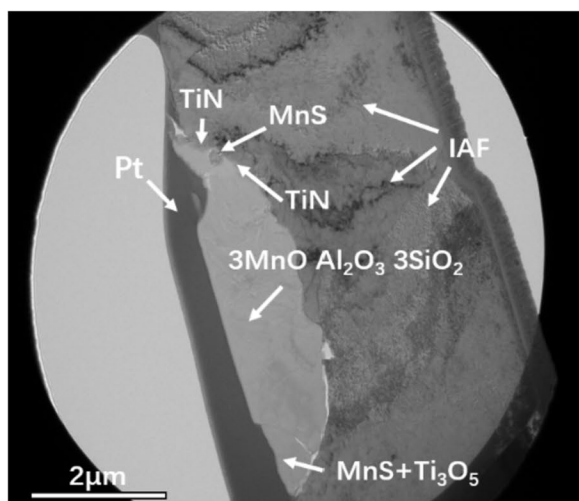


Fig. 10 TEM analysis of whole inclusion inducing AF

Fig. 11 TEM analysis of spherical area. **a** morphology of Inclusion. **b–h** Mapping results. **i** SAED of spherical area

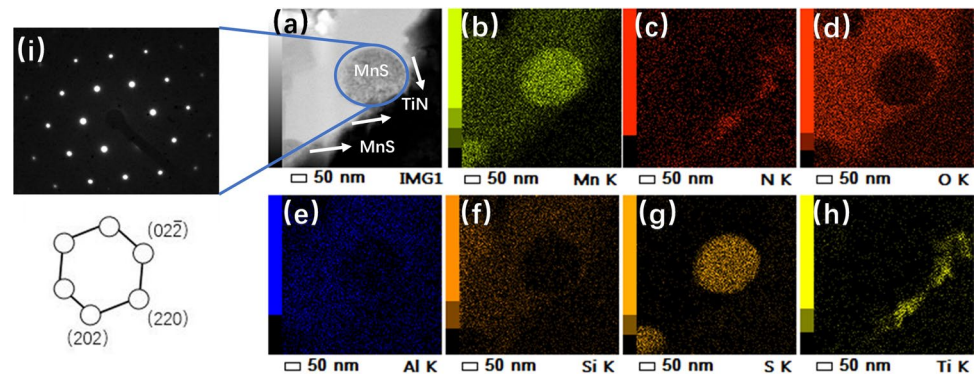


Fig. 12 TEM analysis of triangular area. **a** Morphology of Inclusion. **b–h** Mapping results. **i** SAED of triangular area

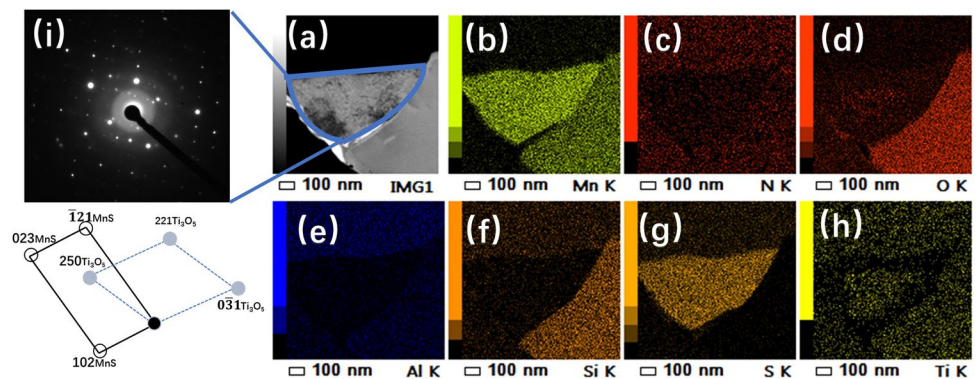
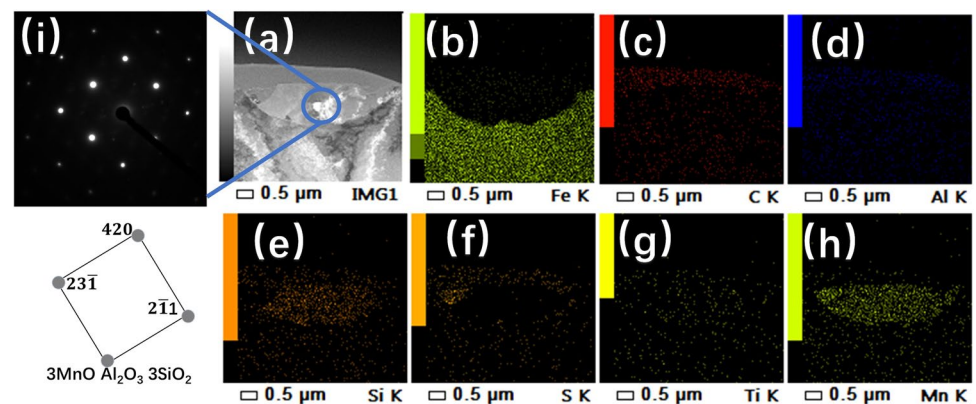


Fig. 13 TEM analysis of central area. **a** Morphology of Inclusion. **b–h** Mapping results. **i** SAED of central area



The spherical inclusion was analyzed by SAED and EDS, as shown in Fig. 11. Mn element has the strongest affinity with S. Notably, there is a good combination between S and Mn. They combine to be spherical inclusion MnS, which is 0.22 μm . The crystal surface is $[1\bar{1}1]$. According to the mapping results, it can be seen that TiN between the composite inclusion and IAF, which conforms to the partial clustering property of Ti. Furthermore, the triangular area (Fig. 12) is MnS + Ti_3O_5 as large as 0.98 μm . MnS diffraction planes are (023), (102), and $(\bar{1}21)$, and Ti_3O_5 diffraction planes are (250), $(\bar{2}21)$, and $(0\bar{3}1)$. Their orientation relationship is MnS $[432]/\text{Ti}_3\text{O}_5 [52\bar{6}]$. An earlier study [24] focused

on the compound inclusion of MnS + Ti_3O_5 can induce IAF nucleation. The middle part of the composite inclusions is $\text{Mn}_3\text{Al}_2\text{Si}_3\text{O}_{12}$ (Fig. 13) and the diffraction planes are $(23\bar{1})$, (420), and (211) . $\text{Mn}_3\text{Al}_2\text{Si}_3\text{O}_{12}$ can be considered as $3\text{MnO} \cdot \text{Al}_2\text{O}_3 \cdot 3\text{SiO}_2$. Calculation of MnO– SiO_2 – Al_2O_3 ternary phase diagram by FactSage6.5 thermodynamic software, the figure is shown in Fig. 14. It can be seen that the inclusion is formed in the low melting point area (gray area) below 1400 $^\circ\text{C}$, with SiO_2 ranging from 0.35 to 0.5%, MnO ranging from 0.2 to 0.5% and Al_2O_3 ranging from 0.15 to 0.3%.

Further, the low lattice misfit mechanism is analyzed. In Fig. 15, there is a gap between $3\text{MnO} \cdot \text{Al}_2\text{O}_3 \cdot 3\text{SiO}_2$

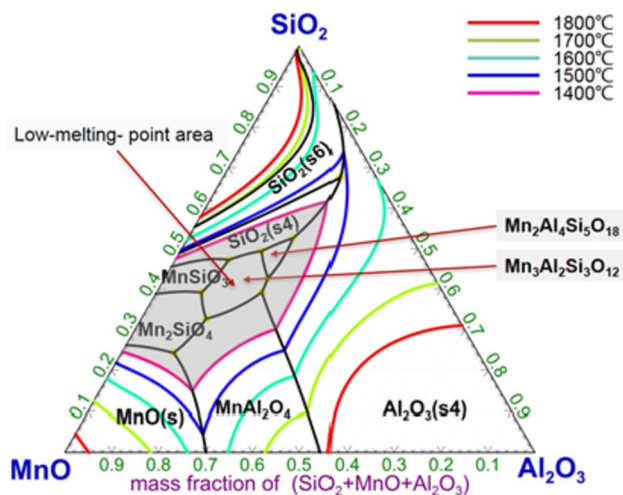


Fig. 14 MnO-Al₂O₃-SiO₂ ternary phase diagram

and IAF. IAF exhibits different interplanar spacings (Fig. 15b) such as $d_{(110)IAF} = 2.03$ nm, $d_{(200)IAF} = 1.43$ nm, and $d_{(721)3MnO \cdot Al_2O_3 \cdot 3SiO_2} = 1.57$ nm or 1.56 nm. Notably, they show good lattice coherency where the inclusion is in close contact with the IAF. Their lattice spacing is similar ($d_{(200)IAF} = 1.43$ nm and $d_{(642)3MnO \cdot Al_2O_3 \cdot 3SiO_2} = 1.57$ nm or 1.56 nm). However, there is a difference in the area of the gap. The orientation relationship is as follows: IAF (200)//3MnO Al₂O₃ 3SiO₂(642). The results prove that good lattice position between 3MnO Al₂O₃ 3SiO₂ and IAF is suitable for the low lattice misfit mechanism. The HREM analysis (Fig. 16) of the spherical MnS + TiN position found that TiN induces the IAF position tightly combining, IAF (221)//TiN (311). As expected that $d_{(201)IAF} = 1.17$ nm is similar to $d_{(311)TiN} = 1.28$ nm.

Based on hexagonal and cubic inclusions, Bramfitt [40] proposed a two-dimensional mismatch degree to characterize and calculate the matching relationship between inclusions and ferrite in steel. The mismatch strain δ can be expressed by the following equation:

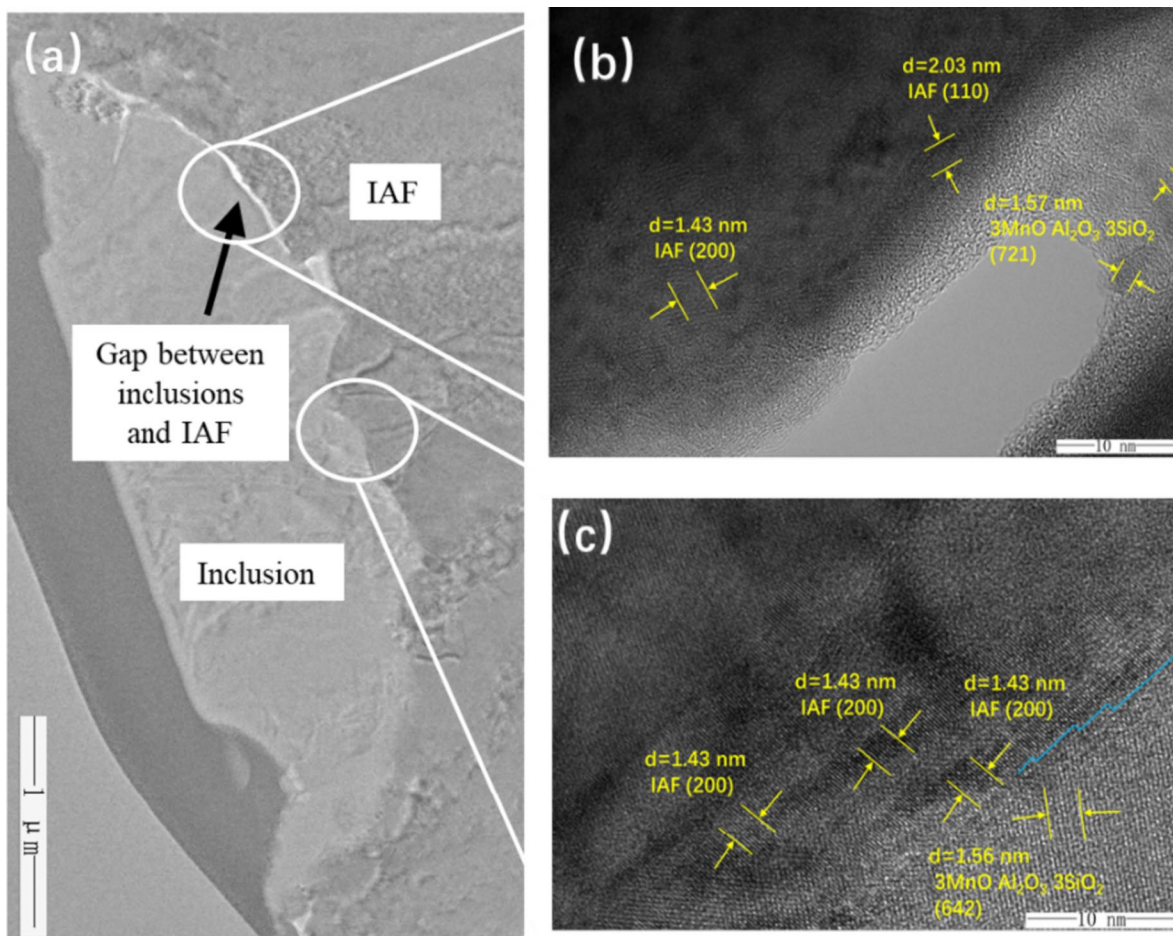
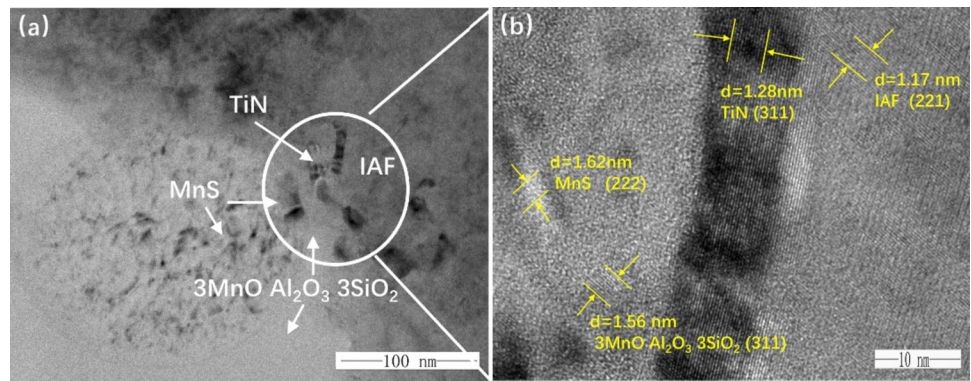


Fig. 15 a Morphology of inclusion inducing AF. b HREM of the gap between 3MnO Al₂O₃ 3SiO₂ and IAF. c HREM of 3MnO Al₂O₃ 3SiO₂ and IAF

Fig. 16 a Morphology of inclusions induced IAF. **b** HREM of inclusions and IAF



$$\delta_{(hkl)_n}^{(hkl)_s} = \sum_{i=1}^3 \frac{|(d_{[uvw]_s}^i \cos \theta) - d_{[uvw]_n}^i|}{3} \times 100\% \quad (2)$$

$(hkl)_s$: low index crystal plane of basal phase; $(hkl)_n$: low index crystal plane of nucleation phase; $[uvw]_s$: crystal plane $(hkl)_s$ with low index; $[uvw]_n$: crystal plane $(hkl)_n$ with low index; $d_{[uvw]_s}$: the atomic spacing along the direction of $[uvw]_s$; $d_{[uvw]_n}$: the atomic spacing along the direction of $[uvw]_n$; δ : the angle between $[uvw]_s$ and $[uvw]_n$.

According to Eq. (2), the smaller the delta value, the more favorable to heterogeneous nucleation. Nucleation is most effective when the mismatch strain, $\delta < 6\%$, is considered moderately effective when δ 6–12% and is not effective when $\delta \geq 12\%$. Table 4 shows that the mismatch strain of the ferrite induced by the known inclusions was calculated. Consequently, δ was less than 6% between the inclusions, TiN, MnS, 3MnO Al₂O₃ 3SiO₂, and Ti₃O₅ as base and IAF nucleation phases, which is effectively nucleation mechanism.

3.4 Stress–Strain Energy

Zhang [41], (Table 5) proposed that during the phase transition, the difference in thermal expansion efficiency between inclusion and austenite can lower the ferrite nucleation barrier, thus increasing ferrite formability. The stress–strain energy equation is as follows:

$$\left(\tau_\gamma = \frac{E_\gamma * E_c}{E_\gamma + E_c} (\alpha_\gamma - \alpha_c) \Delta T \right) \quad (3)$$

$$\varepsilon_\gamma = \frac{\tau_\gamma}{2E_\gamma} \quad (4)$$

E_γ : the young's modulus of austenite; E_c : the young's modulus of inclusion; α_γ : austenite thermal expansion coefficient; α_c : inclusion thermal expansion coefficient; $\Delta T(A_{C3})$: the starting temperature of the temperature gradient form ferrite to austenite.

Table 4 Calculation results of low mismatch (%)

Nucleation phase	Basal phase			
	MnS	TiN	Ti ₃ O ₅	3MnO Al ₂ O ₃ 3SiO ₂
$\delta - Fe$	5.67	3.44	5.86	5.67

Table 5 Inclusion stress–strain energy

Material	Ee (10 ⁴ J/m ³)	Young's elastic modulus (E)	Thermal expansion coefficient (10 ⁻⁶ /°C)
MnS	0.303	103	18.1
TiN	4.14	600	9.4
Ti ₃ O ₅	15.57	350	8.1
austenite	–	210	23

$$A_{C3} = 955 - 350(\text{wt.}\% \text{ C}) - 25(\text{wt.}\% \text{ Mn}) + 51(\text{wt.}\% \text{ Si}) + 100(\text{wt.}\% \text{ Ti}) + 68(\text{wt.}\% \text{ Al}) \quad (5)$$

According to Eq. (5) and Table 1, we calculate $\Delta T = 925.56$ °C. Then, we acquire the form 4 ascribing to Eqs. (3) and (4).

The stress–strain energies of MnS and austenite, TiN and austenite, Ti₃O₅ and austenite are 0.303×10^4 J/m³, 4.14×10^4 J/m³, and 15.57×10^4 J/m³, respectively. However, their order magnitude of stress–strain energy is just 10^4 – 10^5 J/m³, 1/1000 times the driving force for IAF nucleation (10^7 – 10^8 J/m³). That means it is not enough to provide nuclear energy. Nonetheless, only the data of MnS, TiN, and Ti₃O₅ inclusions are listed in this experiment. Computing results are shown without 3MnO Al₂O₃ 3SiO₂ inclusion. The reason is that the crystal structure of 3MnO Al₂O₃ 3SiO₂ is FCC, which is dislocation-free. Owing to its crystallographic characteristics, it cannot stress IAF.

4 Conclusion

This paper studied the influence of TiO₂ on IAF nucleation in low-carbon steel. According to the analysis of the inclusion characteristics (morphology and composition) and how to induce IAF characteristics, the inclusions induce IAF nucleation mechanisms (solute depletion of elements, low lattice misfit, and stress–strain energy). The conclusions are summarized as follows.

- (1) TiO₂ was added to low-carbon steel, forming the composite O–Mn–Si–S–Al–Ti inclusions. Then, O–Mn–Si–S–Al–Ti inclusions induced IAF. The typical inclusions were TiN, MnS, 3MnO Al₂O₃ 3SiO₂, and Ti₃O₅.
- (2) The composite O–Mn–Si–S–Al–Ti inclusion contains Mn elements in the solute poverty zone, and the inclusion is MnS. The induced IAF nucleation can be explained by the solute depletion of elements. The mismatch strain was less than 6% between TiN–MnS–3MnO Al₂O₃ 3SiO₂–Ti₃O₅ and IAF. A low lattice misfit can also clarify that TiN–MnS–3MnO Al₂O₃ 3SiO₂–Ti₃O₅ induces the IAF nucleation.
- (3) For the stress–strain energy mechanism, 3MnO Al₂O₃ 3SiO₂, MnS, TiN, and Ti₃O₅ were insufficient to provide nuclear energy. Mn-depleted zone and low lattice misfit significantly affected TiN–MnS–3MnO Al₂O₃ 3SiO₂–Ti₃O₅ inclusion-induced IAF nucleation.

Declarations

Conflict of interest The authors declare that they have no known competing financial interests or personal relationships that could have appeared to influence the work reported in this paper.

References

1. Turkdogan E T, Ignatowicz S, and Pearson J, *J Iron Steel Res* **180** (1955) 349.
2. Liang W, Geng R, Zhi J, Li J, and Huang F, *Materials* **15** (2022) 1350.
3. Takashi S, Masamitsu W, Yoshiyuki U, and Shozo M, *ISIJ Int* **32** (1992) 169.
4. Sawai T, Wakoh M, and Mizoguchi S, *Tetsu-to-Hagané* **82** (1996) 587.
5. Koseki T, and Thewlis G, *Mater Sci Tech* **21** (2005) 867.
6. Kang Y, Jeong S, Kang J H, and Lee C, *Metall Mater Trans A* **47** (2016) 2842.
7. Byun J S, Shim J H, Suh J Y, Oh Y J, Cho Y W, and Shim J D, *MSEA* **319** (2001) 326.
8. Pan Y T, and Lee J L, *Mater Des* **15** (1994) 331.
9. Wang Y, Wang Q, and Mu W, *Metals* **13** (2023) 517.
10. Homma H, Ohkita S, and Matsuda S, *Weld J* **66** (1987) 301.
11. Takahisa S, Junya I, and Toshihiko K, *ISIJ Int* **47** (2007) 847.

12. Changjoon L, Shoichi N, Junya I, and Toshihiko K, *ISIJ Int* **51** (2011) 2036.
13. Takada A, Komizo Y, Hidenori T, Tomoyuki Y, and Kenji O, *Weld J* **29** (2015) 254.
14. Nambu S, Shibuta N, Ojima M, Inoue J, Koseki T, and Bhadeshia H, *Acta Mater* **61** (2013) 4831.
15. Mu W, Hedström P, and Shibata H, *JOM* **70** (2018) 2283.
16. Yamamoto K, Hasegawa T, and Takamura J I, *ISIJ Int* **6** (1996) 80.
17. Shogo K, Akira N, Kentaro O, and Ken K, *Trans Iron Steel Inst Jpn* **16** (1976) 486.
18. Huang Q, Wang X, Jiang M, Hu Z, and Yang C, *Steel Res Int* **87** (2016) 445.
19. Xiong Z H, Liu S L, Wang X M, Shang C J, Li X C, and Misra R D K, *Mater. Sci. Eng. A* **636** (2015) 117.
20. Sh G, Zhao H, Zhang S, Wang Q, and Zhang F, *Mater Sci Eng A-Struct* **769** (2020) 769.
21. Grong O, Kolbeinsen L, Eijk C V, and Tranell G, *ISIJ Int* **46** (2006) 824.
22. Byun J S, Shim J H, Cho Y W, and Lee D N, *Acta Mater* **51** (2003) 1593.
23. Hou Y, and Cheng G, *Metall Mater Trans B* **50** (2019) 1351.
24. Wang X, Shu W, and Zheng C, *J Univ Sci Technol Beijing* **33** (2011) 958.
25. Song B, Mao J H, Li Y, Wang F, and Luo Z, *Steel Res Int* **08** (2008) 12.
26. Sasaki M, Ohsasa K, Kudoh M, and Matsuura K, *ISIJ Int* **48** (2008) 340.
27. Li X, Wu L, Ma L, and Yan X, *Mech Adv Mater Struct* **26** (2019) 866.
28. Jiang M, Wang X H, and Pak J J, *Metall Mater Trans B* **45** (2014) 1656.
29. Jantzen T, Hack K, Yazhenskikh E, and Müller M, *Calphad* **62** (2018) 187.
30. Wu M, Ren C, Ren Y, and Zhang L, *Metall Mater Trans B* **54** (2023) 1159.
31. Zheng D, Ma G, Zhang X, Liu M, and Li Z, *J Iron Steel Res Int* **28** (2021) 1605.
32. Cai Z, Zhou Y, Tong L, Yue Q, and Kong H, *Mater Test* **57** (2015) 649.
33. Yang Y, Zhan D, and Lei H, *Metall Mater Trans B* **51** (2020) 480.
34. Wang R, Yang J, and Xu L, *Metals* **8** (2018) 946.
35. Noman M T, Ashraf M A, and Ali A, *Environ Sci Pollut Res* **26** (2019) 3262.
36. Qiuping L, Qingjun Z, and Liguang Z, *Mater Rep* **36** (Z1), (2022) 21040258.
37. Sun W P, Militzer M, and Jonas J J, *Metall Trans* **23A** (1992) 821.
38. Fu S, Zhang Y, and Liu H Q, *J Mater Sci Technol* **34** (2018) 335.
39. Liu G, Zhang P, Chong Y, Zhang J, and Sun J, *Acta Metall Sin* **57** (2021) 1484.
40. Bramfitt B L, *Metall Trans* **1** (1970) 2958.
41. Zhang S, Nobuyuki H, Masato E, and Toshimi T, *ISIJ Int* **36** (1996) 1301.

Publisher's Note Springer Nature remains neutral with regard to jurisdictional claims in published maps and institutional affiliations.

Springer Nature or its licensor (e.g. a society or other partner) holds exclusive rights to this article under a publishing agreement with the author(s) or other rightsholder(s); author self-archiving of the accepted manuscript version of this article is solely governed by the terms of such publishing agreement and applicable law.